

EXPLORING GRAVITATIONALLY-LENSED $z \gtrsim 6$ X-RAY AGN BEHIND THE RELICS CLUSTERS

ÁKOS BOGDÁN¹, ORSOLYA E. KOVÁCS^{1,2}, CHRISTINE JONES¹,
WILLIAM R. FORMAN¹, RALPH P. KRAFT¹, VICTORIA STRAIT³, DAN COE⁴, AND MARUŠA BRADAC³
¹Harvard Smithsonian Center for Astrophysics, 60 Garden Street, Cambridge, MA 02138, USA; abogdan@cfa.harvard.edu
²Masaryk University, Kotlarska 2, Brno, 611 37, Czech Republic
³Department of Physics, University of California, Davis, CA 95616, USA and
⁴Space Telescope Science Institute, 3700 San Martin Drive, Baltimore, MD 21218, USA
Draft version November 9, 2021

ABSTRACT

Although observations of high-redshift quasars demonstrate that many supermassive black holes (BHs) reached large masses within one billion years after the Big Bang, the origin of the first BHs is still a mystery. A promising way to constrain the origin of the first BHs is to explore the average properties of $z \gtrsim 6$ BHs. However, typical BHs remain hidden from X-ray surveys, which is due to their relatively faint nature and the limited sensitivity of X-ray telescopes. Gravitational lensing provides an attractive way to study this unique galaxy population as it magnifies the faint light from these high-redshift galaxies. Here, we study the X-ray emission originating from 155 gravitationally-lensed $z \gtrsim 6$ galaxies that were detected in the RELICS survey. We utilize *Chandra* X-ray observations to search for AGN in the individual galaxies and in the stacked galaxy samples. We identify two potential AGN in the high-redshift galaxies, but due to the $\sim 2''$ offset between the X-ray source and the galaxy, we speculate that the X-ray sources are not likely to be associated with the galaxies. We stack the signal from all galaxies and do not find a statistically significant detection. We split our sample based on stellar mass, star-formation rate, and lensing magnification and stack these sub-samples. We obtain a 2.2σ detection for massive galaxies with an X-ray luminosity of $(3.7 \pm 1.6) \times 10^{42}$ erg s⁻¹, which corresponds to a $(3.0 \pm 1.3) \times 10^5 M_\odot$ BH accreting at its Eddington rate. Other stacks remain undetected and we place upper limits on the AGN emission. These limits imply that the bulk of BHs at $z \gtrsim 6$ either accrete at a few percent of their Eddington rate and/or are 1 – 2 orders of magnitude less massive than expected based on the stellar mass of their host galaxy.

Subject headings: galaxies: active — galaxies: high-redshift — galaxies: quasars: supermassive black holes — X-rays: galaxies — X-rays: general — X-rays: galaxies: clusters

1. INTRODUCTION

In the past decades, deep surveys detected more than 200 optically bright quasars at extremely high ($z \gtrsim 6$) redshifts. These discoveries demonstrate that accretion-powered BHs with masses of $\sim 10^9 M_\odot$ were in place merely one billion years after the Big Bang (e.g. Fan et al. 2006; Willott et al. 2007; Jiang et al. 2008; Mortlock et al. 2011; Venemans et al. 2013; Bañados et al. 2014; Wang et al. 2017, 2019; Yang et al. 2017, 2019, 2020). The origin and rapid assembly of BHs can be explained by a number of seeding models, which are usually grouped into “*light seed*” and “*heavy seed*” models. The light seed scenario involves the collapse of Population III stars leading to BH seeds with $10 - 100 M_\odot$ (e.g. Madau & Rees 2001; Volonteri et al. 2003). These low-mass seeds must grow rapidly via accretion and/or mergers to increase their mass by many orders of magnitude in less than one billion years. The heavy seed scenario involves the formation of massive, $10^4 - 10^5 M_\odot$, BHs through the direct collapse of massive gas clouds (e.g. Volonteri & Rees 2005; Begelman et al. 2006; Lodato & Natarajan 2006; Wise et al. 2019). Due to their large initial mass, BHs may grow through episodic accretion, hence this is an attractive model to explain the existence of luminous quasars at $z \gtrsim 6$.

Understanding the origin and early growth of BHs is

arguably one of the most thrilling quests of modern astrophysics. However, to constrain the formation scenarios and early growth of BHs, it is essential to probe BHs residing at high-redshift. Indeed, only these objects can provide the much-needed observational constraints. However, observations of these distant BHs are exceptionally demanding with present-day X-ray observatories. The main difficulty in detecting the “average” high-redshift accreting BHs is due to their low luminosities and the relatively low sensitivity of present-generation X-ray telescopes. Despite the challenging nature, several studies attempted to detect high-redshift BHs in the X-ray waveband. X-ray follow-up of optically-identified quasars led to the detection of high-redshift AGN. Specifically, *Chandra* detected several AGN at $z \sim 6$ (e.g. Ai et al. 2016; Gallerani et al. 2017; Nanni et al. 2017; Vito et al. 2019; Connor et al. 2020; Pons et al. 2020; Wang et al. 2021). The masses of these X-ray-detected BHs is $\sim 10^9 M_\odot$, hence they do not represent the average AGN, which are likely several orders of magnitude less massive. However, these relatively low mass and high-redshift accreting BHs remained hidden from X-ray observations, and, hence our understanding of the average properties of $z \sim 6$ AGN is still lacking despite the substantial efforts over the past decade.

To characterize the average properties of AGN at medium-redshift ($z = 2 - 5$) and high-redshift ($z = 5 - 6$), most studies focused on the *Chandra* Deep Field South

(CDF-S; e.g. Giacconi et al. 2001; Luo et al. 2017). By stacking the X-ray photons of a large number of galaxies, Vito et al. (2016) detected signals from accreting BHs at $z \approx 4$ and $z \approx 5$, but $z \approx 6$ galaxies remained undetected. Recently, Liu et al. (2021) utilized the Cluster Lensing And Supernova survey with Hubble (CLASH) clusters (Postman et al. 2012) to search for AGN in medium- to high-redshift galaxies. They detected a handful of individual AGN in the redshift range of $z = 2.8 - 5$ behind the CLASH clusters and they also stacked their galaxy sample, which led to detections in these redshifts. While these authors demonstrated the feasibility and the powerful nature of using lensing clusters to study high-redshift AGN, their study did not constrain AGN at $z \gtrsim 6$.

In this work, we utilize gravitational lensing that brings into focus fainter sources by magnifying them. Specifically, we rely on the rich X-ray data from the *Chandra X-ray Observatory*, optical data from the *Hubble Space Telescope* (HST), and infrared data obtained from the *Spitzer Space Telescope* for galaxies identified by the Reionization Lensing Cluster Survey (RELICS; Salmon et al. 2020). Through gravitational lensing, these massive galaxy clusters magnify the faint light from high-redshift galaxies behind them. Due to gravitational lensing, only the X-ray photons associated with the source are magnified, while the sky and instrumental background components and – most importantly – the cluster emission is not enhanced. Despite the enhanced signal, the bulk of individual AGN may be too faint to be detected individually. To this end, we boost the signal-to-noise ratios by co-adding (i.e. stacking) the X-ray photons from the individual galaxies. Due to the stacking approach, the combined exposure time will be increased, which allows us to probe the X-ray flux of high-redshift accreting BHs to very low limits. Therefore, this technique could reveal a stacked detection if the individual AGN remain hidden.

This paper is structured as follows. In Section 2 we introduce the analyzed high-redshift galaxy sample and describe its properties. The analysis of the *Chandra* data is described in Section 3. The results of our paper, including the potential individual detections and the detection and upper limits on the stacked samples are presented in Section 4. In Section 5, we place our results into context, where we compare our results with previous studies, and discuss the overall importance of our results. We summarize the results of our study in Section 6. Throughout the paper we assume $H_0 = 70 \text{ km s}^{-1} \text{ Mpc}^{-1}$, $\Omega_M = 0.27$, and $\Omega_\Lambda = 0.73$. The error bars are 1σ uncertainties and the presented upper limits are also 1σ limits.

2. THE ANALYZED GALAXY SAMPLE

The lensing magnification caused by the RELICS clusters provides an incredible opportunity to study extremely high-redshift AGN behind these galaxy clusters. The RELICS survey is a *Hubble Space Telescope* Treasury program (PI: Coe) and a *Spitzer Space Telescope* program (PI: Bradač), which studied 41 massive galaxy clusters that serve as exceptional gravitational lenses. The galaxy clusters reside in the redshift range of $z = 0.18 - 0.97$, which is ideal to utilize the lensing magnification from the clusters and study high-redshift AGN. To study the X-ray emission from the lensed high-redshift AGN, high-resolution X-ray observations with

Chandra are essential. Although *Chandra* did not carry out a systematic study of the RELICS clusters, 35 of the 41 clusters have been observed with *Chandra*. Of these galaxy clusters, we excluded El Gordo (ACT-CLJ0102-49151) whose intracluster medium (ICM) is extremely bright and would outshine possible detections of faint high-redshift AGN and would dominate the overall emission in the galaxy stacks. Therefore, in this work, we study lensed galaxies that are behind the remaining 34 galaxy clusters. The basic properties of this sample are in Table 1.

The detailed analysis of HST and Spitzer data identified 207 galaxies with redshifts of $6 \lesssim z \lesssim 8$ (Strait et al. 2021). Of these galaxies, 174 are behind the studied 34 galaxy clusters. Based on the *HST* and *Spitzer* data, the physical characteristics of the galaxies were computed using two spectral energy distribution (SED) fitting methods. In the first method (dubbed as Method A), the redshift of each galaxy was computed using the Easy and Accurate Redshifts from Yale code (EAZY; Brammer et al. 2008). The resulting photometric redshift probability distribution functions and stellar population synthesis templates were used to calculate the stellar properties of the galaxies. In the second method (dubbed as Method B), the Bayesian Analysis of Galaxies for Physical Inference and Parameter EStimation code (BAGPIPES; Carnall et al. 2018) was used to fit the redshift and the physical properties of the galaxies using the MultiNest nested sampling algorithm. While both of these methods utilize the SED of galaxies, they apply different methodology and template set to obtain the galaxy properties. These differences result in different galaxy properties and distributions of these properties. (for details see Strait et al. 2021). Following Strait et al. (2021), we use the values obtained via Method A as our default throughout this paper. We note that using the redshift fitting procedure of Method A, 19 galaxies were demoted to low redshift systems upon adding the Spitzer fluxes. We excluded these galaxies from our study. Therefore, our final galaxy sample consists of 155 $z \gtrsim 6$ galaxies. In Figure 1, we present the stellar mass, star-formation rate, redshift, and lensing magnification distributions of the 155 lensed galaxies in our sample.

The lensing magnification of the galaxies plays an essential role in our study. In this work, we rely on the magnifications published in Strait et al. (2021). To compute the magnifications, they used three different lens models (if available) to derive lensing maps of the clusters, thereby deriving the lensing magnification for each galaxy. Since the individual lensing magnifications vary, they applied bootstrapping for each lensing model and created multiple lensing constraints for the position of each galaxy. Then the median of these realizations was computed. Since multiple methods were used to obtain the lensing maps, the final lensing magnification was the average of the medians obtained from the different methods. Further details about the analysis are provided in Strait et al. (2021). The derived lensing magnifications are in the range of $\mu = 1 - 95$ with only 10 galaxies having $\mu > 15$. The distribution of magnifications is shown in Figure 1. As a caveat, we note that magnifications $\gtrsim 10$ typically have large uncertainties (Meneghetti et al. 2017), therefore such sources need to be treated with caution.

TABLE 1
 CHARACTERISTICS OF THE GALAXY CLUSTERS ANALYZED IN THIS PAPER

| Cluster name | RA (J2000) | Dec (J2000) | Redshift | Planck mass ($10^{14} M_{\odot}$) | N_{gal} | t_{exp} (ks) |
|--------------|---------------|----------------|----------|--|------------------|--------------------------|
| (1) | (2) | (3) | (4) | (5) | (6) | (7) |
| Abell 1300 | 11:31:54.1 | -19:55:23.4 | 0.307 | 8.97 | 2 | 93.5 |
| Abell 1758 | 13:32:39.0 | +50:33:41.8 | 0.280 | 8.22 | 5 | 213.0 |
| Abell 1763 | 13:35:18.9 | +40:59:57.2 | 0.228 | 8.13 | 8 | 94.5 |
| Abell 2163 | 16:15:48.3 | -06:07:36.7 | 0.203 | 16.12 | 5 | 80.6 |
| Abell 2537 | 23:08:22.2 | -02:11:32.4 | 0.297 | 5.52 | 2 | 74.7 |
| Abell 2813 | 00:43:25.1 | -20:37:14.8 | 0.292 | 8.13 | 1 | 400.3 |
| Abell 3192 | 03:58:53.1 | -29:55:44.8 | 0.425 | 7.20 | 3 | 59.3 |
| Abell 520 | 04:54:19.0 | +02:56:49.0 | 0.203 | 7.80 | 4 | 528.2 |
| Abell 665 | 08:30:57.4 | +65:50:31.0 | 0.182 | 8.86 | 3 | 139.6 |
| Abell 697 | 08:42:58.9 | +36:21:51.1 | 0.282 | 11.0 | 4 | 27.5 |
| Abell S295 | 02:45:31.4 | -53:02:24.9 | 0.300 | 6.78 | 2 | 205.7 |
| CL0152-13 | 01:52:42.9 | -13:57:31.0 | 0.833 | — | 18 | 95.3 |
| MACS0159-08 | 01:59:49.4 | -08:50:00.0 | 0.405 | 7.20 | 3 | 72.7 |
| MACS0025-12 | 00:25:30.3 | -12:22:48.1 | 0.586 | — | 3 | 157.6 |
| RXC0911+17 | 09:11:11.4 | +17:46:33.5 | 0.505 | 6.99 | 3 | 41.7 |
| MACS0035-20 | 00:35:27.0 | -20:15:40.3 | 0.352 | 7.01 | 3 | 21.4 |
| MACS0257-23 | 02:57:10.2 | -23:26:11.8 | 0.505 | 6.22 | 8 | 38.3 |
| MACS0308+26 | 03:08:55.7 | +26:45:36.8 | 0.356 | 10.76 | 4 | 24.4 |
| MACS0553-33 | 05:53:23.1 | -33:42:29.9 | 0.430 | 8.77 | 6 | 84.0 |
| RXC0949+17 | 09:49:50.9 | +17:07:15.3 | 0.383 | 8.24 | 3 | 14.3 |
| RXC2211-03 | 22:11:45.9 | -03:49:44.7 | 0.397 | 10.5 | 2 | 17.7 |
| RXC0018+16 | 00:18:32.6 | +16:26:08.4 | 0.546 | 9.79 | 6 | 67.4 |
| MS1008-12 | 10:10:33.6 | -12:39:43.0 | 0.306 | 4.94 | 8 | 51.2 |
| PLCKG171-40 | 03:12:56.9 | +08:22:19.2 | 0.270 | 10.71 | 2 | 26.7 |
| SMACS0723-73 | 07:23:19.5 | -73:27:15.6 | 0.390 | 8.39 | 6 | 19.8 |
| SPT0615-57 | 06:15:54.2 | -57:46:57.9 | 0.972 | 6.77 | 11 | 241.3 |
| PLCKG287+32 | 11:50:50.8 | -28:04:52.2 | 0.39 | 14.69 | 15 | 196.4 |
| PLCKG138-10 | 02:27:06.6 | +49:00:29.9 | 0.702 | 9.48 | 3 | 11.9 |
| PLCKG209+10 | 07:22:23.0 | +07:24:30.0 | 0.677 | 10.73 | 5 | 10.0 |
| RXC1514-15 | 15:15:00.7 | -15:22:46.7 | 0.223 | 8.86 | 1 | 59.2 |
| RXC0232-44 | 02:32:18.1 | -44:20:44.9 | 0.284 | 7.54 | 2 | 23.4 |
| RXS0603+42 | 06:03:12.2 | +42:15:24.7 | 0.228 | 10.76 | 8 | 237.1 |
| RXC0142+44 | 01:42:55.2 | +44:38:04.3 | 0.341 | 9.02 | 4 | 6.0 |
| PLCKG004-19 | 19:17:04.50 | -33:31:28.5 | 0.520 | 10.36 | 14 | 96.1 |

Columns are as follows. (1) Name of the RELICS cluster; (2) and (3) right ascension and declination of the galaxy cluster; (4) Redshift of the galaxy cluster; (5) Total mass of the galaxy cluster derived from Planck measurements; (6) Number of $z > 5.5$ galaxies behind the galaxy cluster; (7) Total *Chandra* exposure time of the galaxy cluster.

3. ANALYSIS OF THE *CHANDRA* DATA

The analysis of the *Chandra* data was carried out using standard CIAO tools (version 4.13) and the CALDB version 4.9.4. All *Chandra* data were obtained from the public archive. We analyzed 105 high-resolution imaging observations (Table 2). While most of these were taken with ACIS-I array, 8 observations were done with the ACIS-S array. The total exposure time of the observations is 3.53 Ms.

The first step of the analysis was to reprocess all observations. Since the observations were taken in a broad timeframe (from 2000 to 2019), it is essential to apply the same calibration data for each observation. Therefore, we used the *chandra_repro* tool on all observations. Following this step, we filtered the high background time periods. We produced light curves in the 2.3–7.3 keV energy range in 200 s bins and excluded those time periods where the count rate exceeded the mean value by 2σ . Because ACIS-I is only weakly sensitive to high background

periods, the total exposure times were not affected significantly.

To account for vignetting effects, we constructed exposure maps for each observations. Because the main goal of this work is to study the characteristics of high-redshift AGN, we assumed a power law model with a slope of $\Gamma = 1.9$, which is appropriate to describe the spectrum of high-redshift AGN (Nanni et al. 2017). These exposure maps were used to convert the counts to flux units. Since several clusters are observed in multiple pointings, the individual observations and exposure maps were co-added to obtain merged event files and images of the clusters.

Although our main goal is to identify high-redshift AGN, it is expected that there will be many lower redshift AGN in the field-of-view that could contaminate the sample. To identify point sources in the individual galaxy clusters, we used the CIAO *WAVEDETECT* tool. We searched for point sources in the merged images in the

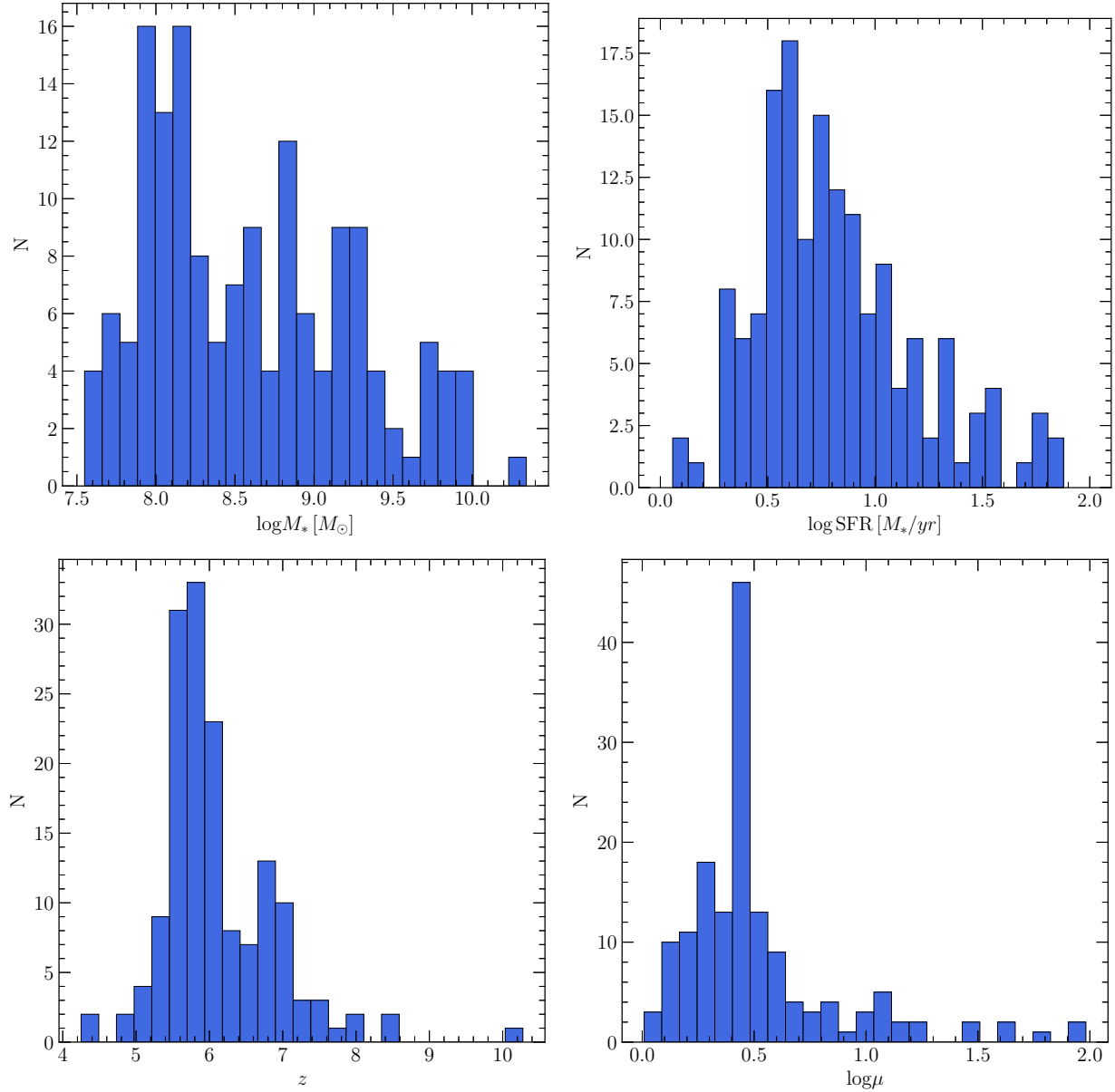


FIG. 1.— Properties of the 155 galaxies analyzed in this work: stellar mass distribution (top left), star formation rate distribution (top right), redshift distribution (bottom left), and median lensing magnification distribution (bottom right). The values are taken from the analysis of Strait et al. (2021) and we relied on their Method A median values to describe the galaxy properties. The lensing magnifications are the median values obtained from different lens models (Section 2).

0.5 – 7 keV (broad band), 0.5 – 2 keV (soft band), and 2 – 7 keV (hard band) energy ranges. We derived point spread function (PSF) maps for each observation using the MKSPFMAP tool, which is used by WAVDETECT to look up the size of the PSF for each pixel in the images. To detect both small and more extended features in the images, we used the square root two series of 2 from $\sqrt{2}$ to 16. In addition, we set the ELLSIGMA parameter to 4, which assures that $\gtrsim 90\%$ fraction of counts associated with the point sources are encircled. Therefore, the residual counts from point sources are not expected to significantly contribute to the large-scale diffuse emission. The resulting source lists were merged and then used to probe whether individual high-redshift AGN at the known coordinates of lensed galaxies are detected in

the *Chandra* images. Finally, we excluded the detected point sources when carrying out the stacking analysis.

We extracted images in the broad, soft, and hard bands. These images were used to cross-correlate the X-ray source list with the galaxy positions and to stack the individual galaxies. To carry out the stacking, we cut out 100×100 pixel regions of the images and exposure maps around each galaxy, and co-added the image and exposure map cutouts.

The lensing magnification affects the fluxes that we observe from the high-redshift AGN. Since the gravitational lensing is achromatic, photons in the optical and X-ray waveband are magnified by the same factor. To account for the magnification factors, we rely on the average lensing magnifications derived by Strait et al.

TABLE 2
LIST OF ANALYZED *Chandra* OBSERVATIONS

| Obs. ID | $t_{\text{exp}}(ks)$ | Detector | Obs. Date | Obs. ID | $t_{\text{exp}}(ks)$ | Detector | Obs. Date |
|---------|----------------------|----------|------------|---------|----------------------|----------|------------|
| 520 | 67.41 | ACIS-I | 2000-08-18 | 14349 | 24.75 | ACIS-I | 2012-11-09 |
| 528 | 9.47 | ACIS-I | 2000-10-10 | 14350 | 11.93 | ACIS-I | 2012-11-21 |
| 531 | 9.01 | ACIS-I | 1999-12-29 | 14351 | 26.23 | ACIS-I | 2012-11-12 |
| 532 | 7.97 | ACIS-I | 1999-10-21 | 14437 | 25.94 | ACIS-I | 2012-09-16 |
| 545 | 9.45 | ACIS-I | 2000-07-29 | 15093 | 111.22 | ACIS-S | 2013-09-12 |
| 913 | 36.48 | ACIS-I | 2000-09-08 | 15094 | 141.20 | ACIS-S | 2013-10-24 |
| 926 | 44.23 | ACIS-I | 2000-06-11 | 15095 | 19.81 | ACIS-S | 2013-09-08 |
| 1653 | 71.15 | ACIS-I | 2001-06-16 | 15171 | 76.57 | ACIS-I | 2013-11-25 |
| 1654 | 19.85 | ACIS-I | 2000-10-03 | 15172 | 111.10 | ACIS-I | 2013-11-28 |
| 2213 | 58.31 | ACIS-S | 2001-08-28 | 15175 | 59.24 | ACIS-I | 2013-04-09 |
| 3251 | 19.33 | ACIS-I | 2002-11-11 | 15296 | 19.82 | ACIS-I | 2014-04-14 |
| 3262 | 21.36 | ACIS-I | 2003-01-22 | 15300 | 9.95 | ACIS-I | 2013-01-28 |
| 3265 | 17.90 | ACIS-I | 2002-10-02 | 15302 | 26.73 | ACIS-I | 2013-09-26 |
| 3268 | 24.45 | ACIS-I | 2002-03-10 | 15323 | 49.43 | ACIS-I | 2013-12-01 |
| 3274 | 14.32 | ACIS-I | 2002-11-06 | 15538 | 93.33 | ACIS-I | 2012-09-28 |
| 3276 | 13.91 | ACIS-I | 2002-06-14 | 15540 | 26.72 | ACIS-I | 2012-10-09 |
| 3284 | 17.74 | ACIS-I | 2002-10-08 | 15572 | 14.86 | ACIS-I | 2012-10-29 |
| 3581 | 18.47 | ACIS-I | 2003-08-23 | 15574 | 13.07 | ACIS-I | 2012-10-31 |
| 3586 | 29.72 | ACIS-I | 2002-12-28 | 15579 | 19.82 | ACIS-I | 2012-11-11 |
| 3587 | 17.88 | ACIS-I | 2003-02-23 | 15582 | 18.34 | ACIS-I | 2012-11-17 |
| 3591 | 19.60 | ACIS-I | 2003-08-28 | 15588 | 23.77 | ACIS-I | 2012-11-22 |
| 4215 | 66.27 | ACIS-I | 2003-12-04 | 15589 | 11.93 | ACIS-I | 2012-11-24 |
| 4217 | 19.52 | ACIS-I | 2002-12-15 | 16127 | 43.32 | ACIS-I | 2014-07-25 |
| 4962 | 36.19 | ACIS-S | 2004-09-09 | 16278 | 8.76 | ACIS-I | 2014-09-17 |
| 4993 | 23.40 | ACIS-I | 2004-06-08 | 16282 | 9.03 | ACIS-I | 2014-06-13 |
| 5010 | 24.83 | ACIS-I | 2004-08-09 | 16366 | 35.60 | ACIS-S | 2013-11-24 |
| 5012 | 23.79 | ACIS-I | 2004-03-08 | 16491 | 34.07 | ACIS-S | 2013-11-19 |
| 5813 | 9.94 | ACIS-I | 2005-01-08 | 16513 | 29.68 | ACIS-S | 2013-11-17 |
| 6106 | 35.30 | ACIS-I | 2004-12-04 | 16524 | 44.60 | ACIS-I | 2014-05-20 |
| 7700 | 5.08 | ACIS-I | 2006-12-30 | 16525 | 44.48 | ACIS-I | 2014-05-17 |
| 7703 | 5.08 | ACIS-I | 2007-01-01 | 16526 | 44.48 | ACIS-I | 2014-08-13 |
| 7710 | 6.97 | ACIS-I | 2007-07-12 | 17165 | 55.35 | ACIS-I | 2015-11-17 |
| 7711 | 6.96 | ACIS-I | 2007-01-13 | 17166 | 20.84 | ACIS-I | 2015-11-24 |
| 9372 | 38.51 | ACIS-I | 2008-08-11 | 17494 | 59.29 | ACIS-I | 2015-08-17 |
| 9376 | 19.51 | ACIS-I | 2008-10-03 | 17495 | 32.23 | ACIS-I | 2016-03-22 |
| 9409 | 19.91 | ACIS-I | 2008-02-02 | 18287 | 11.88 | ACIS-I | 2016-07-19 |
| 9424 | 109.66 | ACIS-I | 2008-01-01 | 18292 | 9.96 | ACIS-I | 2015-12-07 |
| 9425 | 113.52 | ACIS-I | 2007-12-24 | 18466 | 5.99 | ACIS-I | 2016-10-28 |
| 9426 | 110.69 | ACIS-I | 2008-01-09 | 18807 | 28.70 | ACIS-I | 2016-03-23 |
| 9430 | 113.52 | ACIS-I | 2008-01-11 | 19775 | 15.18 | ACIS-I | 2018-03-06 |
| 10413 | 75.64 | ACIS-I | 2008-10-16 | 20590 | 19.69 | ACIS-I | 2019-03-03 |
| 10786 | 13.91 | ACIS-I | 2008-10-18 | 20988 | 19.81 | ACIS-I | 2018-03-08 |
| 10797 | 23.85 | ACIS-I | 2008-10-21 | 20989 | 19.79 | ACIS-I | 2018-03-08 |
| 11719 | 9.65 | ACIS-I | 2009-10-18 | 20990 | 14.88 | ACIS-I | 2018-03-10 |
| 12244 | 74.06 | ACIS-I | 2011-06-23 | 21702 | 35.60 | ACIS-I | 2019-07-30 |
| 12260 | 19.79 | ACIS-I | 2012-01-06 | 21703 | 39.56 | ACIS-I | 2019-09-25 |
| 12286 | 47.10 | ACIS-I | 2012-01-10 | 22130 | 22.76 | ACIS-I | 2019-03-16 |
| 12300 | 29.66 | ACIS-I | 2010-11-26 | 22136 | 12.79 | ACIS-I | 2019-02-24 |
| 13194 | 19.97 | ACIS-I | 2010-11-28 | 22137 | 19.70 | ACIS-I | 2019-03-20 |
| 13201 | 48.71 | ACIS-I | 2011-01-06 | 22679 | 26.71 | ACIS-I | 2019-08-02 |
| 13997 | 27.64 | ACIS-I | 2012-09-27 | 22680 | 33.74 | ACIS-I | 2019-08-04 |
| 14017 | 15.01 | ACIS-I | 2012-11-03 | 22856 | 19.28 | ACIS-I | 2019-09-26 |
| 14018 | 35.60 | ACIS-I | 2012-09-15 | | | | |

(2021), who used a substantial set of lensing models to derive the median magnification factor at the individual galaxy's position and redshift (see Section 2). Because the lensing magnification only affects the emission from

the source and not from the instrumental or sky background, we applied the magnification correction on the background subtracted count rates. Specifically, we multiplied each exposure map associated with the individual

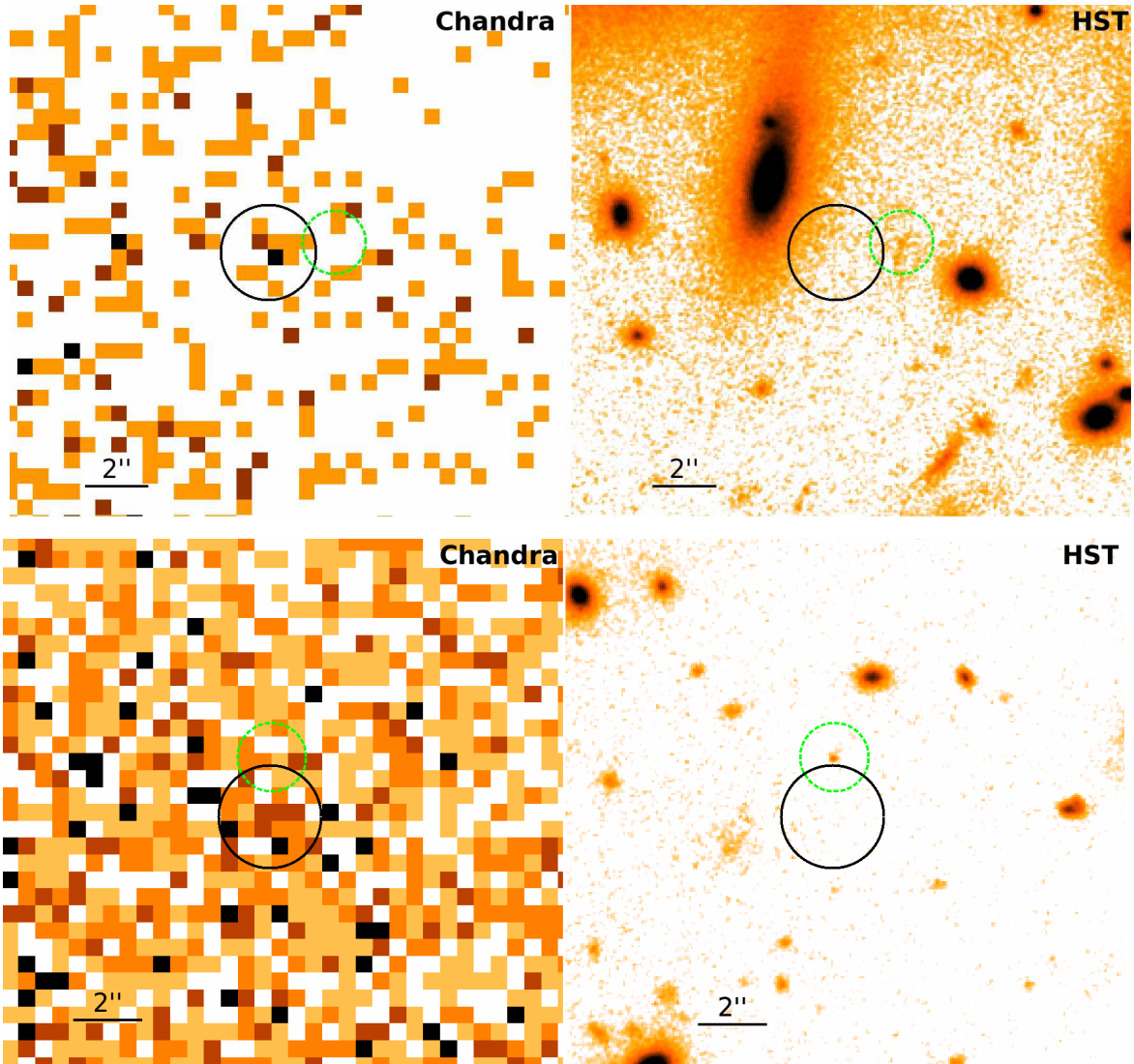


FIG. 2.— The potential matches between the X-ray sources and high-redshift AGN for MAC0553-33 (top panel) and PLCKG287+32 (bottom panel). The left panels show the 0.5 – 7 keV band *Chandra* images and the right panels show the multi-color *HST* images of the regions around the sources. The images are centered on the X-ray sources (black solid circles) that are in the vicinity of galaxies at $z = 6.55$ and $z = 7.82$ (dashed green circles). The projected distances between the centroids of the X-ray point sources and the high-redshift galaxies are 2.1'' and 1.7'' for the source in MAC0553-33 and PLCKG287+32, respectively. However, due to the relatively large projected distance, the X-ray sources are unlikely to be associated with the high-redshift galaxies.

galaxies with the corresponding median lensing magnification taken from Strait et al. (2021). To compute the fluxes and upper limits of the stacked AGN, we used the exposure maps, which were convolved with the lensing magnification.

4. RESULTS

4.1. Individual detections

We first investigated whether the merged *Chandra* images of individual RELICS clusters can detect an AGN associated with the high-redshift galaxies. To this end, we cross-correlated the coordinates of the detected X-ray sources with those of the lensed galaxies. To maximize the likelihood of the search, we carried out the cross-correlation in all three energy ranges. We searched for counterparts within 2.5'' radius. This fairly large search radius was chosen to conservatively account for any differences between the astrometric accuracy of *HST* and

Chandra (Liu et al. 2021) and to consider the broader *Chandra* point spread function at the edges of the detectors.

We identified two X-ray sources, which are in the proximity of high-redshift lensed galaxies. The galaxies are located in MACS0553-33 and PLCKG287+32 and their IDs in the high-redshift galaxy catalog¹ are 830 and 792, respectively. The redshifts of these galaxies are $z = 6.55$ and $z = 7.82$ for IDs 830 and 792. The coordinates and properties of the X-ray source-lensed galaxy pairs are given in Table 3. The offsets between the positions of the X-ray sources and the lensed galaxies are 2.1'' and 1.7'' for MACS0553-33 and PLCKG287+32, which are close to the upper limit of our search radius. Interestingly, the median lensing magnifications at the position

¹ The properties of high-redshift galaxies in Strait et al. (2021) are listed at <https://victoriastrait.github.io/relics>

TABLE 3
INDIVIDUALLY DETECTED X-RAY SOURCES WITH HIGH-REDSHIFT GALAXIES IN THEIR PROXIMITY

| Cluster name | Galaxy ID | RA _X (J2000) | Dec _X (J2000) | RA _{gal} (J2000) | Dec _{gal} (J2000) | z_{gal} | Offset (") | $F_{0.5-7\text{keV}}$ (erg s ⁻¹ cm ⁻²) | $L_{0.5-7\text{keV}}$ (erg s ⁻¹) |
|--------------|-----------|----------------------------|-----------------------------|------------------------------|-------------------------------|------------------|---------------|--|---|
| (1) | (2) | (3) | (4) | (5) | (6) | (7) | (8) | (9) | (10) |
| MACS0553-33 | 830 | 05:53:18.40 | -33:42:38.95 | 05:53:18.23 | -33:42:38.63 | 6.55 | 2.1 | 9.0×10^{-17} | 4.6×10^{43} |
| PLCKG287+32 | 792 | 11:50:48.22 | -28:04:19.62 | 11:50:48.22 | -28:04:17.89 | 7.82 | 1.7 | 4.6×10^{-16} | 3.5×10^{44} |

Columns are as follows. (1) Name of the RELICS cluster; (2) ID number in the RELICS high-redshift galaxy catalog (<https://victoriastrait.github.io/relics>); (3) and (4) Right ascension and declination of the X-ray source; (5) and (6) Right ascension and declination of the high-redshift galaxy in the proximity of the X-ray source; (7) Redshift of the galaxy; (8) Offset between the X-ray source and the high-redshift galaxy; (9) and (10) Flux and X-ray luminosity of the X-ray sources. To compute the luminosity, we assumed that the X-ray source is located at the redshift of the galaxy given in column (7).

of the galaxies are among the largest in our sample: it is $\mu = 16.87$ for the source in MACS0553-33 and $\mu = 9.83$ for PLCKG287+32, respectively.

Assuming that the X-ray sources are associated with the high-redshift galaxies, we estimate their luminosity. We extract the broad band flux of the sources using circular regions with 1" radii and utilized annuli with 2" – 4" radii to subtract the background emission. We convert the observed count rates to flux assuming a power law spectrum with $\Gamma = 1.9$ and Galactic column density. We obtained fluxes of 9.0×10^{-17} erg s⁻¹ cm⁻² for the source in MACS0553-33 and 4.6×10^{-16} erg s⁻¹ cm⁻² for the source in PLCKG287+32. The corresponding X-ray luminosities are 4.6×10^{43} erg s⁻¹ and 3.5×10^{44} erg s⁻¹. Note that these fluxes and luminosities were corrected for the lensing magnification. The obtained values are typical for luminous AGN, such as those detected in the X-ray follow-up studies of optically-identified quasars (Section 5.4).

In Figure 2, we show the broad band *Chandra* and *HST* images of the two X-ray sources and the high-redshift galaxies. The major caveat in the detection of the X-ray source-galaxy pair is the substantial, about 2", offset. At the redshift of the galaxies, the projected offset corresponds to ≈ 11.7 kpc and ≈ 8.5 kpc for the sources in MACS0553-33 and PLCKG287+32, respectively. This projected distance is nearly an order of magnitude larger than the typical half light radius of typical galaxies at $z \sim 6$ (Bouwens et al. 2004), suggesting that the X-ray sources are not associated with the high-redshift galaxies.

Because the offset makes it unlikely that the X-ray sources reside in the high-redshift lensed galaxies, we explore whether the offset can be explained by astrometric uncertainties and discuss alternative origins of the X-ray sources. To probe the accuracy between the *Chandra* and *HST* astrometry, Liu et al. (2021) utilized a sample of bright sources to compute the offsets between the X-ray and optical positions of these sources. They found that the average offset is 0.35" and the largest offset is 0.8". Because the *HST* footprint of MACS0553-33 and PLCKG287+32 contains only a handful of bright X-ray sources, we cannot perform an accurate measurement to establish the offset between the X-ray and optical images. However, inspection of the available sources indicates $< 0.8''$ offset, which is in good agreement with Liu et al. (2021). This result is also not surprising because the absolute astrometry of the RELICS *HST* images were corrected using the *Wide-field Infrared Survey Explorer* point-source catalog (Salmon et al. 2020). Thus, it is unlikely that the offset between the galaxy and

the X-ray source is due to differences in the *Chandra* and *HST* astrometry.

If the X-ray sources are not associated with the high-redshift lensed galaxies and have a physical origin (i.e. are not spurious detections²), the X-ray counts may arise from three different sources. First, the X-ray sources may be associated with other nearby galaxies. To probe this possibility, we checked if there are other galaxies at lower redshifts in the proximity of the X-ray sources. Analysis of the RELICS clusters³ identified two more luminous (21 mag and 23 mag) galaxies at $z \sim 0.4$, which lie at a projected distance of $\sim 4''$ (~ 21 kpc). Although this projected distance is larger than the optical extent of the galaxies, it cannot be excluded that the luminous X-ray sources are associated with these galaxies. In this case, the luminosity of the sources is in the range of few times 10^{41} erg s⁻¹, implying that they may be ultraluminous X-ray sources (Swartz et al. 2011; Kaaret et al. 2017). Second, it is possible that the X-ray sources belong to extremely faint high-redshift ($z \gtrsim 6$) galaxies. Faint galaxies at such redshifts could remain undetected due to the limited sensitivity of *HST* in the infrared and the relatively low angular resolution and collecting area of *Spitzer*. The high lensing magnification at the position of the X-ray sources, which may have drastically magnified the X-ray images, make this scenario appealing. However, to probe this possibility, it will be crucial to observe these lensing clusters with the *James Webb Space Telescope* that will simultaneously deliver the much-needed infrared sensitivity and large collecting area, allowing the detection of faint and high-redshift galaxies. Third, it is also feasible that the X-ray sources do not originate from distant galaxies, but are internal to the galaxy cluster. In this case, the sources may originate from high density clumps in the ICM, which could appear as point sources in the X-ray images. To differentiate between these scenarios, it would be necessary to collect deeper X-ray data that can characterize the energy spectrum of the sources and to explore the lensing galaxy clusters with *JWST*.

The other X-ray sources in our sample do not have a high-redshift galaxy in their proximity. This suggests that most point sources are associated with AGN at lower redshifts or they may be foreground objects.

4.2. Stacking the high-redshift galaxies

² To understand the origin of spurious detections of point sources in X-ray images, we refer to the CIAO WAVEDETECT manual: <https://cxc.cfa.harvard.edu/ciao/threads/wavdetect/>.

³ <https://relics.stsci.edu/data.html>

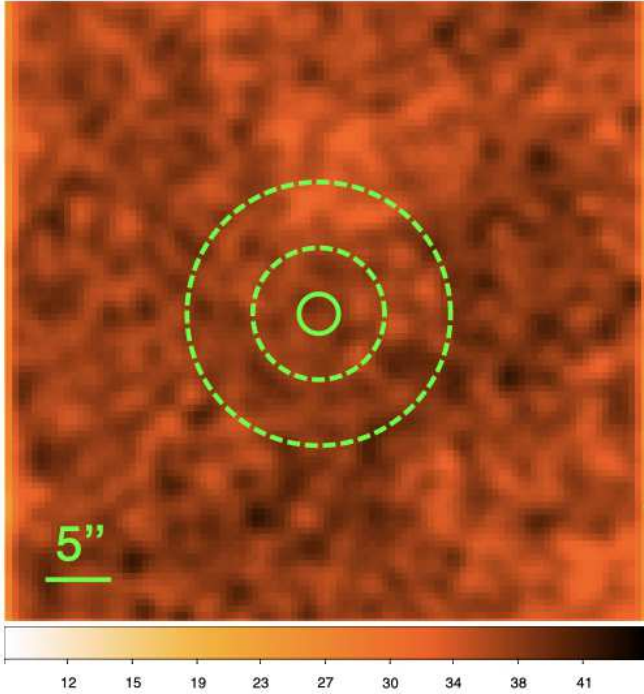


FIG. 3.— Stacked 0.5 – 7 keV band image of the 155 galaxies in our sample. The stacked sample does not reveal a statistically significant detection. The source and background regions used to derive the upper limits are shown with the circle (solid line) and annulus (dashed lines).

To increase the signal-to-noise ratios and the likelihood of detecting high-redshift AGN, we stacked the X-ray photons associated with the individual galaxies. This approach, combined with the lensing magnifications, allows us to probe relatively faint AGN. Indeed, the sensitivity of our study is nearly compatible with that achieved in the 7 Ms Chandra Deep Field South regions (see Section 5.2).

A major difference between the present work and previous stacking analyses (e.g. Vito et al. 2016) is that we are co-adding galaxies that reside behind rich galaxy clusters. Therefore, emission from the intracluster medium (ICM) contributes to the overall emission and elevates the background level. In addition, the ICM exhibits notable structure across galaxy clusters, particularly in merging systems. In our analysis, we do not specifically account for the varying level of ICM emission associated with the individual lensed galaxies. Because the regions that were cut around individual galaxies are small (Section 3) relative to the angular size of the galaxy clusters, variations in the ICM emission are negligible on these small scales and average out across the stacked images.

We carried out the stacking analysis in all three energy ranges using multiple approaches. First, we co-added all 155 galaxies in our sample. The visual inspection of the stacked image (Figure 3), does not reveal a bright point source at the center of the image. To constrain the flux associated with the stacked AGN, we extracted the counts from the stacked image and applied the stacked lensing-corrected exposure maps. The source and background regions were described with a circular region with $1.5''$ radius and with an annulus with

$5'' - 10''$ radii, respectively. We did not detect a statistically significant signal associated with the stacked high-redshift AGN. In the absence of a detection, we place an upper limit on the flux. Taking into account the lensing-corrected exposure maps, the upper limit on the flux is $F_{0.5-2\text{keV}} < 2.1 \times 10^{-18} \text{ erg s}^{-1} \text{ cm}^{-2}$, which corresponds to a luminosity of $L_{0.5-2\text{keV}} < 9.1 \times 10^{41} \text{ erg s}^{-1}$ using the mean redshift of $z = 6.11$.

Although the entire galaxy sample does not reveal a detection, we further split our sample to increase the likelihood of a detection. We used three criteria to divide our sample. First, we split the galaxies based on their stellar mass. It is well established that stellar bulge mass of galaxies is proportional with the BH mass in the local Universe (e.g. McConnell & Ma 2013; Saglia et al. 2016). Recently, this correlation was investigated for dwarf galaxies and it was found that the $M_{\text{BH}} - M_{\text{bulge}}$ relation can be extended to these low mass galaxies (Schutte et al. 2019). While this relation may be different for galaxies at $z \sim 6$, it is reasonable to assume that more massive galaxies, even at the low-mass regime, host more massive BHs, which, in turn, are expected to shine brighter as AGN. Hence, by dividing our sample by mass, we expect that the average luminosity of AGN in the high-mass sample will become detectable. The luminosity of AGN in low-mass galaxies will be lower than that of the entire sample, implying that this sample will remain undetected. To split the sample based on mass, we applied $4 \times 10^8 M_{\odot}$ as our threshold, which approximately splits our sample into two equal-sized groups. After stacking the galaxies in the two sub-samples, we obtained a 2.2σ detection in the high-mass sample, while the low-mass sample remained undetected (Figure 4). We derive fluxes of $F_{0.5-2\text{keV}} = (8.1 \pm 3.6) \times 10^{-18} \text{ erg s}^{-1} \text{ cm}^{-2}$ and $F_{0.5-2\text{keV}} < 2.5 \times 10^{-18} \text{ erg s}^{-1} \text{ cm}^{-2}$ for the two samples, which correspond to $L_{0.5-2\text{keV}} = (3.7 \pm 1.6) \times 10^{42} \text{ erg s}^{-1}$ and $L_{0.5-2\text{keV}} < 1.0 \times 10^{42} \text{ erg s}^{-1}$. We further discuss this possible detection in Section 5.

The second approach to split the galaxies into two samples was based on the star formation rate. It is believed that the stellar population of galaxies co-evolves with their central BH as they are feeding from the same gas supply (e.g. Hopkins et al. 2006). This, in turn, suggests that galaxies with high star formation rate may host BHs that are growing at a more rapid pace hence are more luminous. Additionally, galaxies with high star-formation rates are expected to host a more numerous population of high-mass X-ray binaries, whose total luminosity is proportional to the star formation rate of the host galaxy (Mineo et al. 2012). Finally, actively star-forming galaxies are also more likely to host ultraluminous X-ray sources, which can have luminosities comparable to low-luminosity AGN (Kovlakas et al. 2020). Taken all together, galaxies with high star-formation rate may exhibit a higher X-ray luminosity and could be detected in the stacked sample. We split our galaxy sample into two groups using $4 M_{\odot} \text{ yr}^{-1}$ as the threshold. We did not detect a statistically significant signal from either sub-samples. Therefore, we derived 1σ upper limits on the fluxes and luminosities of the galaxies.

As the third approach, we split the galaxy sample based on their median lensing magnification. The advantage of this method is that the lensing magnification only

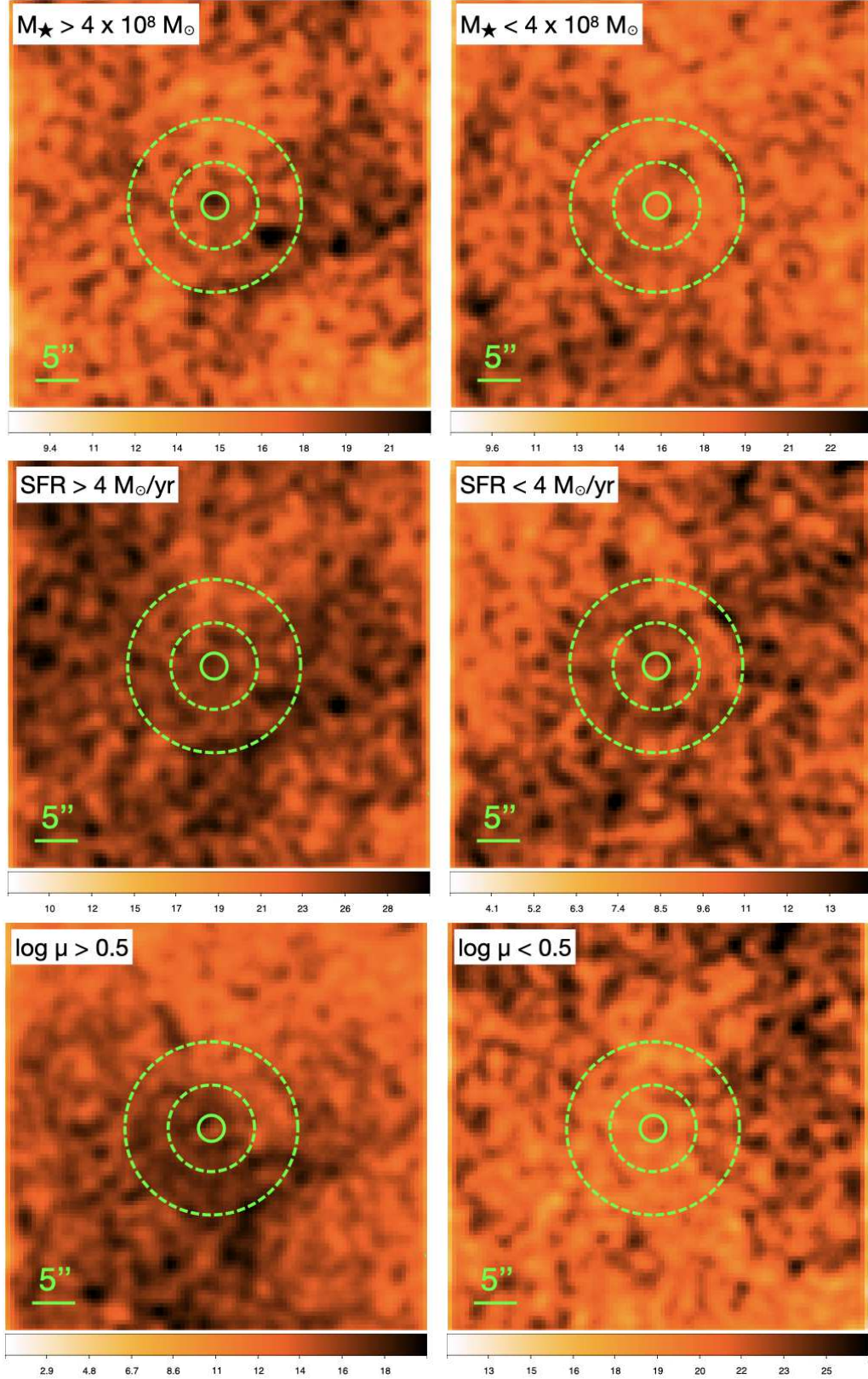


FIG. 4.— Stacked 0.5–7 keV band *Chandra* images of lensed high-redshift galaxies using different binning criteria. We split the galaxies based on stellar mass (top row), star-formation rate (middle), and lensing magnification (bottom). We obtained a weak, 2.2σ detection for the high-mass sub-sample, while other sub-samples remained undetected. The physical criteria to divide the galaxies into bins is shown on the stacked images.

boosts the signal from the high-redshift galaxies (i.e. the luminosity of the AGN), while it does not increase the galaxy cluster emission and the overall background level. Hence, the high lensing magnification sample should result in improved signal-to-noise ratios from the AGN. We selected $\log \mu = 0.5$ as our threshold to split the galaxies. After stacking the two sub-samples and measuring the count rates, we found that none of the two sub-samples exhibit detections. Therefore, we derived upper limits on the flux and luminosity of the AGN.

We present the stacked images in Figure 4 and we tabulated the results of the stacking analysis in Table 4. This table includes the number of galaxies, fluxes, and luminosities for each sub-sample. While we relied on Method A to split the galaxies into sub-samples, for completeness we also list the mean physical properties of the galaxies obtained through Method B. The results are further discussed in Section 5.

5. DISCUSSION

5.1. Monte Carlo simulations

In Section 4.1 we identified two X-ray sources that reside in the vicinity of high-redshift lensed galaxies. Given the large number of X-ray sources detected on the *Chandra* images, it is possible that the association is due to coincidence. In this case, the X-ray sources may be AGN residing in other galaxies or could be due to dense clumps in the ICM. To estimate the likelihood of random matches, we carried out Monte Carlo simulations.

In the Monte Carlo simulations, we generated random coordinates within the footprint of the galaxy clusters. For each cluster, the number of random coordinates was the same as the number of high-redshift galaxies in the given cluster. Based on these sets of coordinates, we carried out the same analysis as described in Section 4.1 and searched for matches between the simulated “high-redshift galaxies” and the X-ray sources. Similarly to the real data, we utilized a search radius of $2.5''$. To obtain a statistically meaningful sample, we generated 10,000 random sets of “high-redshift” galaxies, which amount to a total of $155 \times 10^4 = 1.55 \times 10^6$ randomly selected coordinates.

We identified 2,373 random matches for all these coordinates, which corresponds to a likelihood of $\approx 0.15\%$ chance coincidences. Based on the 155 high-redshift galaxies studied in our sample, we expect ≈ 0.23 random matches. Therefore, the identification of two matches within $2.5''$ in our observed data set is at the upper end of the predictions. This, in turn, implies that one or possibly even two X-ray sources are associated with either a high-redshift galaxy or belongs to a foreground galaxy and is not the result of coincidence.

5.2. Comparison with CDF-S

So far the most powerful constraints on the average properties of high-redshift AGN were obtained by Vito et al. (2016), who carried out a stacking analysis using the deep, 7 Ms, observations of the Chandra Deep Field South field. Vito et al. (2016) stacked AGN in three redshift bins: $3.5 < z < 4.5$, $4.5 < z < 5.5$, and $5.5 < z < 6.5$. They obtained statistically significant detections for the two lower redshift bins, but AGN in the highest redshift bin remained undetected. Due to the

large galaxy sample and the deep observations, the total stacked exposure time of galaxies in the $5.5 < z < 6.5$ redshift bin was about 1.35×10^9 s and the derived flux upper limit was $< 4.4 \times 10^{-19}$ erg s $^{-1}$ cm $^{-2}$, which corresponds to a luminosity of $< 1.8 \times 10^{41}$ erg s $^{-1}$ assuming $z = 6$ (Table 4).

Although the number of high redshift galaxies in our sample is similar to that studied in Vito et al. (2016), the stacked exposure time of the galaxies in the RELICS sample is nearly two orders of magnitude shorter and is about 2.0×10^7 s. However, the lensing magnification of the galaxy clusters significantly improves our signal-to-noise ratios. Since the gravitational lensing is achromatic, it increases the signal from the high-redshift galaxies but not the background emission (including the X-ray emission originating from the intracluster medium).

Similarly to the galaxies in CDF-S, we also did not detect a statistically significant signal from high-redshift galaxies when stacking all galaxies in the sample. The $0.5 - 2$ keV band flux upper limits are about a factor of ~ 4 times higher than those obtained in the CDF-S footprint. Similarly to Vito et al. (2016), we divided our sample based on the stellar mass of the host galaxies. Interestingly, we obtained a weak ($\sim 2.2\sigma$) detection in the stacked galaxy sample, with fluxes of 8.1×10^{-18} erg s cm $^{-2}$, which exceeds the CDF-S flux upper limit by factor of ~ 8 . However, due to the relatively low signal-to-noise ratio of the detection, we cannot exclude that this detection is an upward fluctuation. This detection is further discussed in the next Section.

5.3. Detection in the high-mass sub-sample

Our sample of massive high-redshift galaxies exhibited a 2.2σ detection. The corresponding X-ray flux is factor of about 8 times higher than the upper limit obtained for $z \sim 6$ galaxies in the CDF-S field. This result may appear controversial, especially when comparing the stellar masses of the galaxies in the CDF-S and RELICS samples. The median stellar mass of the RELICS galaxies is lower than that of the CDF-S galaxies (Table 4). However, this difference is likely due to systematic effects associated with the determination of stellar masses at high redshifts.

The SED fitting of the CDF-S galaxies was done by ten independent teams (Santini et al. 2015). The stellar masses presented in Vito et al. (2016) correspond to the median of the stellar masses obtained from these ten different groups. At $z < 5.5$, the stellar mass estimates obtained through different methods are in good agreement with each other. However, at high redshift ($5.5 < z < 6.5$) there are large differences, which are mostly caused by the inclusion (or omission) of nebular line emission in the models. Specifically, only three teams included the nebular line emission in their SED fitting procedure, which, however, is essential to accurately fit the SED of high redshift galaxies. Indeed, emission lines, such as H- β and [OIII] can substantially contaminate the observed rest-frame window and drastically alter the SED fitting. The net effect of this is that the stellar mass of high redshift galaxies can be over-estimated. According to Santini et al. (2015), the omission of nebular lines in young and/or high-redshift galaxies can result in stellar masses that are overestimated by up to a factor of 25. Based on Santini et al. (2015), we estimate that not

TABLE 4
 PROPERTIES OF THE STACKED SAMPLES

| Bin | N_{gal} | z | μ | M_* (#A) (M_{\odot}) | M_* (#B) (M_{\odot}) | SFR (#A) ($M_{\odot} \text{ yr}^{-1}$) | SFR (#B) ($M_{\odot} \text{ yr}^{-1}$) | $F_{\text{obs},0.5-2\text{keV}}$ ($\text{erg s}^{-1} \text{ cm}^{-2}$) | $L_{\text{obs},0.5-2\text{keV}}$ (erg s^{-1}) |
|------------------------|------------------|------|-------|-------------------------------|-------------------------------|---|---|---|---|
| (1) | (2) | (3) | (4) | (5) | (6) | (7) | (8) | (9) | (10) |
| High-mass | 73 | 6.22 | 3.6 | 2.6×10^9 | 4.7×10^9 | 16.8 | 22.0 | $(8.1 \pm 3.6) \times 10^{-18}$ | $(3.7 \pm 1.6) \times 10^{42}$ |
| Low-mass | 82 | 6.01 | 7.9 | 1.4×10^8 | 9.2×10^8 | 4.4 | 3.8 | $< 2.5 \times 10^{-18}$ | $< 1.0 \times 10^{42}$ |
| High-SFR | 105 | 6.17 | 5.8 | 1.8×10^9 | 3.6×10^9 | 13.7 | 16.7 | $< 2.7 \times 10^{-18}$ | $< 1.1 \times 10^{42}$ |
| Low-SFR | 50 | 5.99 | 6.2 | 2.6×10^8 | 8.3×10^8 | 3.0 | 3.2 | $< 3.3 \times 10^{-18}$ | $< 1.4 \times 10^{42}$ |
| $\log \mu > 0.5$ | 48 | 6.37 | 13.8 | 1.3×10^9 | 3.1×10^9 | 10.6 | 17.3 | $< 2.6 \times 10^{-18}$ | $< 1.2 \times 10^{42}$ |
| $\log \mu < 0.5$ | 107 | 5.99 | 2.4 | 1.3×10^9 | 2.5×10^9 | 10.1 | 10.1 | $< 3.4 \times 10^{-18}$ | $< 1.4 \times 10^{42}$ |
| All RELICS | 155 | 6.11 | 5.91 | 1.3×10^9 | 2.7×10^9 | 10.3 | 12.3 | $< 2.1 \times 10^{-18}$ | $< 9.1 \times 10^{41}$ |
| All CDF-S [†] | 230 | 5.93 | – | $(0.2 - 60.1) \times 10^9$ | | $(1.1 - 328.7)$ | | $< 4.4 \times 10^{-19}$ | $< 1.8 \times 10^{41}$ |

[†] All galaxies in the CDF-S field with $5.5 < z < 6.5$. The stellar mass and star formation rates for the CDF-S galaxies are based on Santini et al. (2015). Because these values were *not* computed following the method described in Strait et al. (2021), we opt to show the range of these parameters.

Columns are as follows. (1) Binning method; (2) Number of galaxies in the bin; (3) Mean redshift of galaxies; (4) Median lensing magnification factor; (5) and (6) Mean stellar mass of galaxies obtained via Methods A and B in Strait et al. (2021), respectively; (7) and (8) Mean star-formation rate of galaxies computed via Methods A and B in Strait et al. (2021); (9) and (10) Observed flux and luminosity of the galaxies in the 0.5 – 2 keV band, respectively.

accounting for nebular emission lines will result in factor of ~ 3 too high stellar masses for the overall $5.5 < z < 6.5$ galaxy population with $\sim 15\%$ of the galaxies having a factor of ~ 5 too high stellar masses. Since the stellar masses presented in Santini et al. (2015) are the median⁴ of the values obtained by the different teams and most of the teams did not include emission from the nebular emission lines, the stellar masses for $5.5 < z < 6.5$ galaxies presented in Santini et al. (2015) and employed in Vito et al. (2016) are over-estimated.

As opposed to this, nebular emission lines were included in the SED fitting procedure for the RELICS galaxies (Strait et al. 2021), which therefore provide more accurate stellar masses. Thus, the large offset between the stellar masses of the CDF-S and RELICS samples can be explained with the different SED fitting methods, in particular by the inclusion of nebular emission lines. Taking this difference into account, it is feasible that the RELICS high-mass sample includes – on average – more massive galaxies than the CDF-S field. In addition, we note that in the present work we utilize the stellar masses obtained through Method A in Strait et al. (2021). However, the stellar masses derived through Method B are systematically higher than those in Method A; for example for the high-mass sample the stellar masses are factor of ~ 2 higher (Figure 5). Therefore, the stacked detection of high-redshift galaxies behind the RELICS clusters is not incompatible with the non-detection of high-redshift galaxies in the CDF-S field. Indeed, the analysis of Vito et al. (2016) pointed out for the $3.5 < z < 5.5$ stacked samples that the detected X-ray signal from AGN is most sensitive to the stellar mass of the host galaxies and the most massive galaxies dominate the signal.

To further probe whether the derived 2.2σ detection may be caused by a chance coincidence, we carried out Jackknife resampling. To this end, we randomly selected 73 high-redshift galaxies (which is identical with the number of galaxies in the high-mass bin) from the sample, co-added the X-ray photons associated with them,

and derived the detection significance. We repeated this analysis 10^5 times to obtain a statistically meaningful sample. The detection significances of the randomly stacked galaxies shows a normal distribution that has a peak detection significance distribution at $\approx 0.16\sigma$. We found that only $\approx 0.3\%$ of the random resampling simulations show $\geq 2.2\sigma$ detections. This is less frequent than that suggested by the 2.2σ detections, hinting that the detection in the massive high-redshift galaxies is unlikely to be the result of chance coincidence.

5.4. Comparison with individual detections

Over the past decades, wide-area optical and infrared surveys identified a substantial population (> 200) of extremely luminous quasars at $z > 5.5$ (e.g. Fan et al. 2006; Willott et al. 2007; Jiang et al. 2008; Mortlock et al. 2011; Venemans et al. 2013; Bañados et al. 2014; Wang et al. 2017, 2019; Yang et al. 2017, 2019, 2020). A fraction of these sources were followed up using X-ray observatories, which allowed the determination of the X-ray properties of these high-redshift AGN. For example, Nanni et al. (2017) presented a systematic study of 29 quasars at $z > 5.5$ that were observed by *Chandra*, *XMM-Newton*, or *Swift*-XRT. They established that the 0.5 – 2 keV band X-ray luminosity of these sources ranges from several times $10^{43} \text{ erg s}^{-1}$ to a few times $10^{45} \text{ erg s}^{-1}$.

Clearly, the luminosity of the quasars studied in Nanni et al. (2017) surpasses the X-ray upper limits obtained in our stacking analysis by about 1.5 – 3.5 orders of magnitude. This demonstrates that the individually studied luminous quasars represent the bright tip of the luminosity function, and are not representative of the general AGN population at $z \sim 6$. Although the source detection sensitivity strongly varies in our galaxy cluster sample due to the different exposure times and spatially varying lensing magnifications, we estimate the typical detection sensitivity of our study. To this end, we rely on the average *Chandra* exposure time ($t_{\text{exp}} = 104 \text{ ks}$) of the RELICS galaxy cluster sample (Table 1), use the median lensing magnification factor of $\mu = 3$, apply the median redshift ($z = 5.9$) of the lense galaxies, and assume that an X-ray AGN can be detected with 10 counts.

⁴ The median of the stellar masses in Santini et al. (2015) was computed using the Hodges-Lehmann estimator.

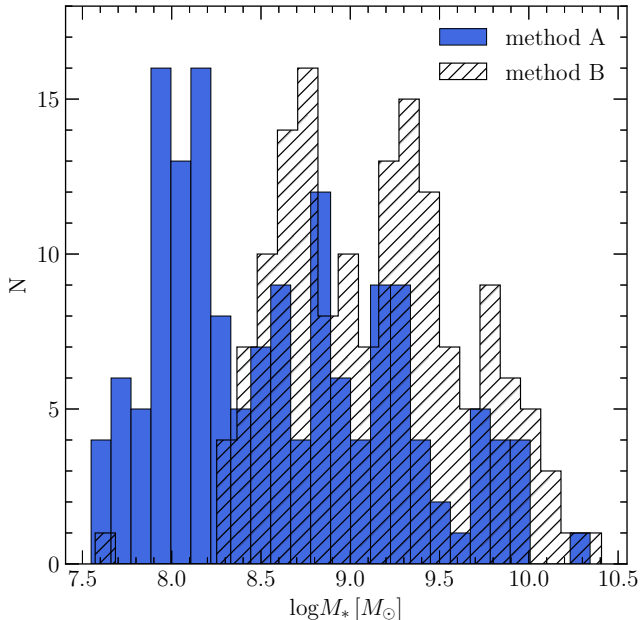


FIG. 5.— Stellar mass distribution of the 155 high-redshift galaxies obtained using the two different SED fitting methods described in Strait et al. (2021). In this work, we rely on the stellar masses derived using their Method A. The stellar masses obtained through Method B are systematically higher. Note that both SED fitting methods include nebular line emission.

We thus obtain an average source detection sensitivity of $\sim 10^{44}$ erg s $^{-1}$, which implies that the bulk of the quasars in the sample of Nanni et al. (2017) could be individually detected behind the RELICS clusters.

In the sample of RELICS galaxies, we identified two X-ray sources that *may be* associated with $z \sim 6$ galaxies – see the caveats in Section 4.1. Taking these two potential X-ray source-galaxy pairs as upper limits, we find that $< 1\%$ of $z \sim 6$ galaxies host AGN with luminosities of $\gtrsim 4 \times 10^{43}$ erg s $^{-1}$. This result is also in line with our stacking analysis, which suggests that no more than a few per cent of galaxies may host AGN with such high luminosities.

5.5. High mass X-ray binaries

Although the primary goal of our study is to constrain the X-ray emission from luminous high-redshift AGN, other sources also contribute to the overall X-ray emission. Most notably, high-mass X-ray binaries also present a major source of X-ray emission. The X-ray emission from these sources is proportional to the star formation rate of the galaxy. Taking into account the L_X -SFR relation established in Mineo et al. (2012), the redshift evolution of the relation (Lehmer et al. 2016), and assuming a power law slope with $\Gamma = 2$, the average expected 0.5 – 2 keV band luminosity from HMXBs is 1.4×10^{41} erg s $^{-1}$.

This average HMXB luminosity is about an order of magnitude below our detection limit. Therefore, given the sensitivity of our stacking analysis, it is unlikely that HMXBs can be detected in the present data set, even in our high-SFR sub-sample. Therefore, the non-detection of X-ray emission from HMXBs is consistent with the estimated X-ray luminosity from these sources. As a

caveat, we note that the L_X -SFR scaling relation has only been probed in the redshift range of $z = 1 - 4$ and it cannot be excluded that $z \approx 6$ galaxies exhibit a different relation. However, based on the observed redshift evolution of this relation, it seems unlikely that their contribution will be close to the sensitivity of our stacking analysis.

The predicted X-ray luminosity associated with high-redshift galaxies with the highest star-formation rates ($\sim 100 M_\odot$ yr $^{-1}$) is about 1.5×10^{42} erg s $^{-1}$. While these luminosities are comparable with the average sensitivity of the stacks, these values remain below the individual source detection limits, which is also consistent with the fact that none of the galaxies with high star-formation rate were individually detected on the *Chandra* images. The metallicity of galaxies strongly influences the number of HMXBs (e.g. Linden et al. 2010; Lehmer et al. 2016). Specifically, the number of HMXBs per unit stellar mass is significantly higher in galaxies with low ($\sim 20\%$) metallicities (Douna et al. 2015), with the excess sources being mostly present at the bright end of the X-ray luminosity function (Lehmer et al. 2021). While the effect of decreasing metallicity at higher redshift galaxies was incorporated in the model of Lehmer et al. (2016), galaxies with extremely low metallicities and high star-formation rates could be individually detected in other lensed high-redshift galaxies. Additionally, future, more sensitive X-ray surveys will be able to detect the X-ray emission from HMXBs in high-redshift galaxies.

5.6. Constraining the properties of $z \sim 6$ BHs

Based on the data from the stacked galaxies, we can constrain the characteristics of the *typical* $z \sim 6$ AGN. The X-ray upper limit on the luminosity of the BHs in the RELICS galaxy sample is $L_X < 8.4 \times 10^{41}$ erg s $^{-1}$ (Table 4). Assuming a bolometric correction of $K_{\text{bol}} = 10$ (Lusso et al. 2012), the upper limit on the bolometric luminosity is $L_{\text{bol}} < 8.4 \times 10^{42}$ erg s $^{-1}$. If BHs accrete at their Eddington rate, this upper limit corresponds to a mean BH mass of $M_{\text{BH}} < 6.7 \times 10^4 M_\odot$. Clearly, this average BH mass is about 4 orders of magnitude lower than those detected in the most luminous quasars.

If we assume that galaxies at $z \sim 6$ obey the BH mass–bulge mass scaling relation obtained in the local Universe (Schutte et al. 2019) and consider the mean stellar mass of our sample ($1.3 \times 10^9 M_\odot$), we expect a mean BH mass of $M_{\text{BH}} = 2.6 \times 10^6 M_\odot$. This implies that the BH mass calculated from the mean stellar mass is ~ 40 times larger than the upper limit assuming Eddington accretion. Thus, our results imply that BHs are either much less massive at $z \sim 6$ than expected from the local scaling relation or they accrete at a few per cent of their Eddington rate. We note that the former possibility is incompatible with some observational studies. Specifically, Merloni et al. (2010) suggested that BHs at high redshift may be over-massive relative to their host galaxies, and Bogdán et al. (2012) hinted that some BHs may grow faster than their host galaxies at high redshift. However, the relatively low mean accretion rate is feasible if most BHs originate from the heavy seed scenario. In this picture, BHs may experience episodic periods with high accretion rates, while most times they accrete at low Eddington rates.

Performing a similar calculation for the high-mass sub-sample that has a weak X-ray detection results in the same conclusion. The bolometric X-ray luminosity for these BHs is $L_{\text{bol}} = 3.7 \times 10^{42} \text{ erg s}^{-1}$, which corresponds to a mean BH mass of $M_{\text{BH}} = 3.0 \times 10^5 M_{\odot}$ assuming Eddington accretion. The average stellar mass of our high-mass sample is $2.6 \times 10^9 M_{\odot}$, which would imply that the mean BH mass is $6.5 \times 10^6 M_{\odot}$ if they follow the local scaling relation. The latter value is ~ 22 times lower than that obtained assuming the Eddington accretion rate. Therefore, it is likely that even the more massive BHs do not accrete at the Eddington limit, but the average accretion rate remains at the $\sim 5\%$ level.

The low average accretion rate is not surprising when compared to theoretical studies. Most of the BH accretion, and hence BH growth, is expected to happen in the most luminous AGN and it is expected that BHs with low accretion rates will have a small contribution to the overall BH growth. For example, Volonteri et al. (2016) established, based on the Horizon-AGN simulations, that at high-redshifts ($z > 4$), the bulk of the BH growth takes place in the most luminous ($L_{\text{bol}} > 10^{44} \text{ erg s}^{-1}$) and most rapidly accreting ($f > 0.1 f_{\text{Edd}}$) AGN. Because the sensitivity of our stacking analysis is well below this limit, the non-detection of the AGN in the full stacked RELICS galaxy sample is consistent with this. Since the observed luminosity of AGN depends both on the Eddington ratio and the BH mass, the detection of AGN in the high-mass galaxy sub-sample may be attributed to the more massive BH sample even though the mean accretion rates are still low.

5.7. Obscuration

A fraction of AGN remains hidden behind gas and dust that absorbs the emission from the accretion disk of the BH. Because the obscured fraction of AGN may depend on both the luminosity and the redshift, our understanding of the complete census and evolution of AGN depends on the obscured fraction of AGN. A wide range of studies explored the obscuration of high-redshift AGN, which found that about 50% of $3 < z < 6$ AGN are obscured by a column density $N_H > 10^{23} \text{ cm}^{-2}$ (Vito et al. 2013, 2018; Hickox & Alexander 2018).

To assess the importance of obscuration, we follow Vito et al. (2016) and assume that 50% of the AGN are obscured by a column density of $N_H = 3.2 \times 10^{23} \text{ cm}^{-2}$ and assume that all sources have the same intrinsic luminosity. Given these conditions, the transmission factor for typical $z = 6$ AGN is $c = 0.3$, yielding a correction factor of $F_{0.5-2\text{keV},\text{total}}/F_{0.5-2\text{keV},\text{obs}} = 1.3$. While this factor is not applied for the observed X-ray fluxes and luminosities, the total – obscuration corrected – fluxes and luminosities can be computed by using this correction factor.

5.8. Outlook

This work represents the first attempt to utilize gravitational lensing to constrain the average characteristics of AGN in $z \sim 6$ galaxies. We obtained a 2.2σ detection of galaxies in the high-mass sub-sample, while other sub-samples remained undetected. This initial result is encouraging: it emphasizes the powerful nature of our approach and highlights that future detections with higher statistical significance are feasible.

To further advance our understanding of high-redshift AGN, the advancement of both optical/infrared observatories and deeper X-ray observations are required. *JWST* will completely revolutionize our understanding of the early Universe by detecting large samples of faint and high-redshift galaxies. Two instruments aboard *JWST*, the Near InfraRed Camera (NIRCam) and the Mid InfraRed Instrument (MIRI), will provide broadband photometry that will allow probing the rest-frame UV, optical, and near-infrared spectral energy distributions of high-redshift galaxies. Thanks to its large collecting area, superb angular resolution, and infrared sensitivity, *JWST* will explore a vast population of galaxies at $z = 6 - 10$ and will even identify the first galaxies at $z \sim 15$. By utilizing existing, upcoming, and proposed deep *Chandra* observations of lensed galaxy clusters, the sample of high-redshift AGN can be significantly increased, thereby improving the signal-to-noise ratios, which may lead to further detection of AGN and/or the population of HMXBs in distant galaxies, both individually and in stacks.

On a longer timescale, more sensitive high-resolution X-ray telescopes could provide an edge in detecting high-redshift galaxies that were identified by *JWST*. For example, the proposed *Lynx* observatory would be able to reach sensitivities to even individually detect some of the lensed AGN and would be able to probe the average luminosity of HMXBs. Indeed, *Lynx* could drastically change the landscape of high-redshift AGN studies as it will detect AGN with luminosities with $10^{41} \text{ erg s}^{-1}$ in deep fields and at even lower luminosities by utilizing the lensing magnification of galaxy clusters. While *JWST* and *Lynx* would not operate simultaneously, X-ray follow-up observations of *JWST* targets will revolutionize our understanding about high-redshift AGN.

6. CONCLUSIONS

In this work, we analyzed *Chandra* X-ray observations of 34 RELICS galaxy clusters and probed the X-ray emission originating from 155 gravitationally-lensed galaxies that reside at $z \gtrsim 6$. We probed the emission from high-redshift AGN both individually and in stacks. Our results can be summarized as follows:

- To search for individually detected AGN associated with the high-redshift galaxies, we cross-matched the coordinates of the detected X-ray sources with those of the lensed galaxies. We identified two potential matches, but due to the $\sim 2''$ offset we suggest that the X-ray sources are not likely to be associated with the lensed galaxies.
- To probe the average X-ray luminosity from high-redshift galaxies, we co-added the X-ray signal from the 155 lensed galaxies, but did not obtain a statistically significant detection. In the absence of detection, we placed a flux upper limit on the high-redshift AGN, which was $< 2.1 \times 10^{-18} \text{ erg s}^{-1} \text{ cm}^{-2}$, which corresponds to a luminosity upper limit of $< 8.4 \times 10^{41} \text{ erg s}^{-1}$.
- Assuming that $z \sim 6$ galaxies follow the local BH mass–bulge mass scaling relation, we estimate that the typical BH mass is $\sim 6.7 \times 10^5 M_{\odot}$. Given the upper limit on the luminosity, this implies that

typical BHs at high redshift accrete at 5 – 10% of their Eddington rate.

- We split galaxies based on their stellar mass, star-formation rate, and lensing magnification and stacked galaxies in these sub-samples. We obtained a weak, 2.2σ , detection for massive galaxies. Taken at face value, the luminosity of the AGN in the high-mass group is $3.7 \times 10^{42} \text{ erg s}^{-1}$. We did not obtain a statistically significant detection in other sub-samples.
- We find that emission from HMXBs is well below the sensitivity of the stacking analysis given the star-formation rate of the sample.

Acknowledgements. The scientific results reported in this article are based to a significant degree on data obtained from the Chandra Data Archive. This research has made use of software provided by the Chandra X-ray Center (CXC) in the application packages CIAO, ChIPS, and Sherpa. This work is based on observations taken by the RELICS Treasury Program (GO 14096) with the NASA/ESA HST, which is operated by the Association of Universities for Research in Astronomy, Inc., under NASA contract NAS5-26555. Á.B., C.J., W.R.F. and R.K. acknowledge support from the Smithsonian Institution and the Chandra High Resolution Camera Project through NASA contract NAS8-03060. O.E.K. is supported by the GACR EXPRO grant No. 21-13491X. M.B. and V.S. acknowledge support provided by NASA/HST grant HST-GO-15920.

REFERENCES

- Ai, Y., Dou, L., Fan, X., et al. 2016, *ApJ*, 823, L37
- Bañados, E., Venemans, B. P., Morganson, E., et al. 2014, *AJ*, 148, 14
- Begelman, M. C., Volonteri, M., & Rees, M. J. 2006, *MNRAS*, 370, 289
- Bogdán, Á., Forman, W. R., Zhuravleva, I., et al. 2012, *ApJ*, 753, 140
- Bouwens, R. J., Illingworth, G. D., Blakeslee, J. P., Broadhurst, T. J., & Franx, M. 2004, *ApJ*, 611, L1
- Brammer, G. B., van Dokkum, P. G., & Coppi, P. 2008, *ApJ*, 686, 1503
- Carnall, A. C., McLure, R. J., Dunlop, J. S., & Davé, R. 2018, *MNRAS*, 480, 4379
- Connor, T., Bañados, E., Mazzucchelli, C., et al. 2020, *ApJ*, 900, 189
- Douna, V. M., Pellizza, L. J., Mirabel, I. F., & Pedrosa, S. E. 2015, *A&A*, 579, A44
- Fan, X., Strauss, M. A., Richards, G. T., et al. 2006, *AJ*, 131, 1203
- Gallerani, S., Zappacosta, L., Orofino, M. C., et al. 2017, *MNRAS*, 467, 3590
- Giacconi, R., Rosati, P., Tozzi, P., et al. 2001, *ApJ*, 551, 624
- Hickox, R. C., & Alexander, D. M. 2018, *ARA&A*, 56, 625
- Hopkins, P. F., Hernquist, L., Cox, T. J., et al. 2006, *ApJS*, 163, 1
- Jiang, L., Fan, X., Annis, J., et al. 2008, *AJ*, 135, 1057
- Kaaret, P., Feng, H., & Roberts, T. P. 2017, *ARA&A*, 55, 303
- Kovlakas, K., Zezas, A., Andrews, J. J., et al. 2020, *MNRAS*, 498, 4790
- Lehmer, B. D., Basu-Zych, A. R., Mineo, S., et al. 2016, *ApJ*, 825, 7
- Lehmer, B. D., Eufrasio, R. T., Basu-Zych, A., et al. 2021, *ApJ*, 907, 17
- Linden, T., Kalogera, V., Sepinsky, J. F., et al. 2010, *ApJ*, 725, 1984
- Liu, A., Tozzi, P., Rosati, P., et al. 2021, *arXiv e-prints*, arXiv:2102.05788
- Lodato, G., & Natarajan, P. 2006, *MNRAS*, 371, 1813
- Luo, B., Brandt, W. N., Xue, Y. Q., et al. 2017, *ApJS*, 228, 2
- Lusso, E., Comastri, A., Simmons, B. D., et al. 2012, *MNRAS*, 425, 623
- Madau, P., & Rees, M. J. 2001, *ApJ*, 551, L27
- McConnell, N. J., & Ma, C.-P. 2013, *ApJ*, 764, 184
- Meneghetti, M., Natarajan, P., Coe, D., et al. 2017, *MNRAS*, 472, 3177
- Merloni, A., Bongiorno, A., Bolzonella, M., et al. 2010, *ApJ*, 708, 137
- Mineo, S., Gilfanov, M., & Sunyaev, R. 2012, *MNRAS*, 419, 2095
- Mortlock, D. J., Warren, S. J., Venemans, B. P., et al. 2011, *Nature*, 474, 616
- Nanni, R., Vignali, C., Gilli, R., Moretti, A., & Brandt, W. N. 2017, *A&A*, 603, A128
- Pons, E., McMahon, R. G., Banerji, M., & Reed, S. L. 2020, *MNRAS*, 491, 3884
- Postman, M., Coe, D., Benítez, N., et al. 2012, *ApJS*, 199, 25
- Saglia, R. P., Opitsch, M., Erwin, P., et al. 2016, *ApJ*, 818, 47
- Salmon, B., Coe, D., Bradley, L., et al. 2020, *ApJ*, 889, 189
- Santini, P., Ferguson, H. C., Fontana, A., et al. 2015, *ApJ*, 801, 97
- Schutte, Z., Reines, A. E., & Greene, J. E. 2019, *ApJ*, 887, 245
- Straat, V., Bradač, M., Coe, D., et al. 2021, *ApJ*, 910, 135
- Swartz, D. A., Soria, R., Tennant, A. F., & Yukita, M. 2011, *ApJ*, 741, 49
- Venemans, B. P., Findlay, J. R., Sutherland, W. J., et al. 2013, *ApJ*, 779, 24
- Vito, F., Vignali, C., Gilli, R., et al. 2013, *MNRAS*, 428, 354
- Vito, F., Gilli, R., Vignali, C., et al. 2016, *MNRAS*, 463, 348
- Vito, F., Brandt, W. N., Yang, G., et al. 2018, *MNRAS*, 473, 2378
- Vito, F., Brandt, W. N., Bauer, F. E., et al. 2019, *A&A*, 630, A118
- Volonteri, M., Dubois, Y., Pichon, C., & Devriendt, J. 2016, *MNRAS*, 460, 2979
- Volonteri, M., Haardt, F., & Madau, P. 2003, *ApJ*, 582, 559
- Volonteri, M., & Rees, M. J. 2005, *ApJ*, 633, 624
- Wang, F., Wang, R., Fan, X., et al. 2019, *ApJ*, 880, 2
- Wang, F., Fan, X., Yang, J., et al. 2017, *ApJ*, 839, 27
- . 2021, *ApJ*, 908, 53
- Willott, C. J., Delorme, P., Omont, A., et al. 2007, *AJ*, 134, 2435
- Wise, J. H., Regan, J. A., O’Shea, B. W., et al. 2019, *Nature*, 566, 85
- Yang, J., Fan, X., Wu, X.-B., et al. 2017, *AJ*, 153, 184
- Yang, J., Wang, F., Fan, X., et al. 2019, *AJ*, 157, 236
- . 2020, *ApJ*, 897, L14